Article

Not peer-reviewed version

Role of Morphology in Phase-Engineered TiO_2 Nanostructures: Comparative Assessment of Anatase and Brookite for Emerging Aqueous Pollutant Degradation and NOx Abatement

Humaira Asghar * , Daphne Hermosilla , Francesco Pellegrino , Antonio Gascó , Valter Maurino ,
Muhammad Ahsan Iqbal

Posted Date: 23 March 2025

doi: 10.20944/preprints202503.1649.v1

Keywords: shape controlled titanium dioxide (TiO_2); photocatalytic degradation; aqueous pollutants; NOx abatement

Preprints.org (www.preprints.org) | NOT PEER-REVIEWED | Posted: 23 March 2025 doi:10.20944/preprints202503.1649.v1

Article

Role of Morphology in Phase-Engineered TiO_2 Nanostructures: Comparative Assessment of Anatase and Brookite for Emerging Aqueous Pollutant Degradation and NOx Abatement

Humaira Asghar [1,*], Daphne Hermosilla [2], Francesco Pellegrino [1], Antonio Gascó [2], Valter Maurino [1] and Muhammad Ahsan Iqbal [3]

[1] Department of Chemistry, University of Torino, Via Giuria 7, 10125 Torino, Italy
[2] G-Aqua Research Group, Departamento de Ingeniería y Gestión Forestal y Ambiental, Universidad Politécnica de Madrid, José Antonio Novais 10, 28040 Madrid, Spain
[3] Departamento de Ingeniería Química y de Materiales, Facultad de Ciencias Químicas, Universidad Complutense de Madrid, 28040 Madrid, Spain
* Correspondence: email: humaira.asghar@unito.it

Abstract: This study investigates the synthesis of shape-controlled titanium dioxide (TiO_2) nanoparticles via a hydrothermal method, examining the influence of pH variation (8, 10, 12, and 14) and subsequent thermal treatments (200°C and 230°C) on phase transitions and morphological transformations. The resulting TiO_2 nanostructures—including nanorods, nanotubes, nanoflowers, elongated bipyramids, and irregular flower-like assemblies—undergo phase transitions from anatase to brookite. Their photocatalytic performance is assessed for aqueous pollutant degradation and NOx abatement. TiO_2 synthesized at lower pH (8-10), exhibiting anatase-phase nanotubular and elongated bipyramidal morphologies, achieves near-complete photodegradation of phenol, methomyl, and diclofenac in both Milli-Q and stormwater matrices. Conversely, brookite-rich TiO_2 phases, formed at higher pH (12-14), show limited liquid-phase activity but excel in NOx abatement, making them promising candidates for air purification applications. These findings highlight the pivotal role of phase composition and morphology in optimizing photocatalytic performance, offering a strategic approach for the scalable development of efficient TiO_2-based photocatalysts for environmental remediation.

Keywords: Titanium dioxide (TiO_2), Controlled morphologies; Photocatalytic degradation; Aqueous pollutants; NOx abatement

1. Introduction

Environmental pollution, particularly from emerging aqueous contaminants and airborne nitrogen oxides (NOx), presents a growing global challenge. Pharmaceuticals, pesticides, and industrial chemicals persist in aquatic ecosystems, leading to bioaccumulation and long-term ecological risks [1,2]. Simultaneously, NOx emissions from industrial activities contribute to air quality deterioration, acid rain formation, and respiratory diseases [3–5]. Addressing these issues requires the development of advanced, efficient photocatalytic materials for sustainable pollutant remediation.

Titanium dioxide (TiO_2) is a widely studied photocatalyst due to its high stability, non-toxicity, and strong photocatalytic activity under UV light [6–9]. However, its practical applications are often constrained by a wide band gap and limited visible-light activity. To enhance its performance, strategies such as doping, surface modification, and morphology control have been explored. Among these, shape-controlled synthesis of TiO_2 nanostructures has proven effective in optimizing photocatalytic efficiency by increasing surface area, promoting charge separation, and improving light absorption [10–19]. Different crystal faces can be exposed by controlling the size and shape of photocatalytic materials at the nanoscale, each with distinct surface states and catalytic properties.

This underscores the crucial role of synthesis parameters in optimizing TiO_2 properties for specific applications. Our recent work demonstrated the significant impact of shape-controlled TiO_2 nano cuboids and TiO_2 nanobelts heterostructures as highly effective nanocatalysts for efficiently mineralizing a broad range of pollutants [19,20].

Despite advancements in TiO_2-based photocatalysis, a comprehensive understanding of how synthetic parameters influence morphology and phase transitions (anatase, brookite) remains limited. While anatase is widely recognized for its superior photocatalytic efficiency in aqueous pollutant degradation, brookite has shown promise for NOx abatement due to its enhanced catalytic performance in gaseous reactions [21]. This study systematically investigates the role of pH and thermal treatment in tailoring TiO_2 morphology and phase composition, with an emphasis on its impact on photocatalytic applications in both liquids (Phenol, methomyl, diclofenac)- and gas-phase pollutant (NOx) removal.

2. Materials and Methods

2.1. Materials

P25 (EVONIK), NaOH (Beijing Chemicals, purity > 96.0%), deionized water (Milli-Q system), and stormwater (collected from a collection center in Madrid, Spain) were used in the study. Methanol and orthophosphoric acid (HPLC grade) were purchased from Scharlab (Barcelona, Spain) for chromatographic analysis. The pesticide methomyl (99.5% purity) was obtained from Aragonesas Agro S.A. (Madrid, Spain). Sodium diclofenac (DCF, >99% purity) and phenol (99% purity) were provided by Aldrich (Darmstadt, Germany). Table S1 (Supplementary Data) lists the general characteristics of the pollutants investigated, and Table S2 presents the chemical characteristics of alkaline stormwater.

2.2. Synthesis of Na-titanate

A total of 3.5 g of P25 was dispersed in 140 mL of 10 M NaOH aqueous solution and transferred to a 200 mL Teflon-lined stainless-steel autoclave. The mixture was heated at 120°C for 24 hours, followed by air cooling, resulting in the formation of white Na-titanate precipitates. These precipitates were isolated by centrifugation and repeatedly washed with deionized water. The washing process was continued while adjusting the pH using NaOH solution to achieve final pH values of 14, 12, 10, and 8. The resulting Na-titanate powder was separated by centrifugation and freeze-dried overnight.

2.3. Synthesis of shape-controlled brookite and anatase TiO_2

Na-titanates (1 g), synthesized at different pH values (14, 12, 10, and 8), were individually dispersed in 40 mL of deionized water and transferred to a 50 mL Teflon-lined stainless-steel autoclave. The mixtures were subjected to hydrothermal treatment at two different temperatures, 200°C and 230°C, for 24 hours, followed by natural air cooling, resulting in the formation of white TiO_2 precipitates. These precipitates were isolated by centrifugation, thoroughly washed with deionized water, and freeze-dried overnight.

The specimens were labelled based on their synthesis conditions as pH(X)-Y(°C), where "X" represents the pH value used during synthesis, and "Y" denotes the thermal treatment temperature. Initial trials at temperatures above 230°C led to phase instability, causing undesirable transitions to rutile, which disrupted the selective formation of anatase and brookite—key phases of interest in this study. To mitigate this, reaction temperatures were optimized to 200°C and 230°C, ensuring controlled phase formation while preserving the desired surface morphologies. Figure 1 illustrates the synthesis route of the developed TiO_2 nanostructures.

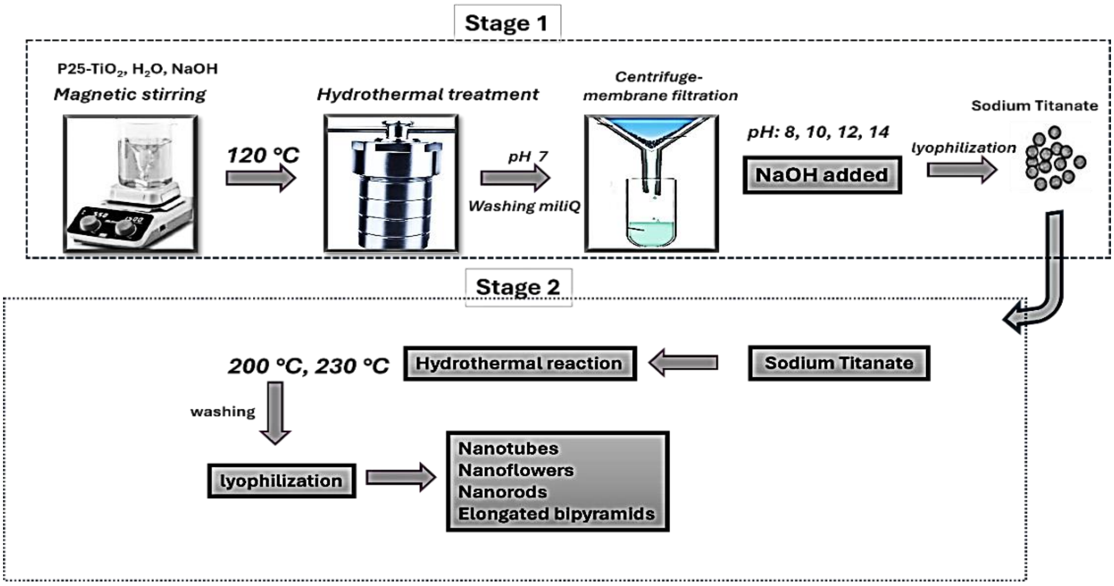

Figure 1. Schematic route of the preparation of the shape-controlled TiO_2 nanoparticles.

3. Characterization

3.1. Physical Characterization

Morphological and microstructural features were examined using a JEOL-IT300 scanning electron microscope (SEM). X-ray diffraction (XRD) patterns were obtained with a Rigaku X'Pert High Score diffractometer (Japan) under ambient conditions, utilizing cobalt K-α radiation (λ = 1.54 Å) at 10 mA and 30 kV. Measurements were performed with a step size of 0.005° over a 2θ range of 20° to 80°. UV-visible diffuse reflectance spectra (DRS) were collected using a Shimadzu UV-Vis-NIR spectrophotometer (Model UV-3600) at room temperature, with a wavelength range from 200 to 800 nm.

3.2. Photocatalytic degradation of aqueous pollutants

A series of controlled experiments were conducted to assess the photocatalytic activity of the synthesized catalyst. Suspensions containing 1 g/L of the catalyst were placed in a photoreactor and exposed to ultraviolet (UVA) light from ten LED lamps (Seoul Viosys, Republic of Korea) emitting at 385 nm. The LEDs were arranged to ensure uniform illumination across the reactor surface, each operating at 250 mA with a power consumption of 8.38 W. The photon flux, measured using the potassium ferrioxalate actinometry method, was determined to be 1682.8 ± 77.1 µmol m^2 s^{-1}.

Photocatalytic degradation of pollutants was monitored by tracking concentration changes of initial 0.1 mM solutions, with degradation kinetics analyzed using an exponential decay model. Experiments were conducted under natural pH conditions. Before irradiation, the reaction mixture was stirred in the dark for 30 minutes to establish adsorption equilibrium. During irradiation, 0.8 mL aliquots were collected at specific intervals, filtered through a 0.45 µm nylon filter to remove suspended catalyst particles, and analyzed. Pollutant concentrations were determined using high-performance liquid chromatography (HPLC) equipped with a diode array detector, a binary gradient pump, and an automated sampler. After 120 minutes of irradiation, total organic carbon (TOC) content was measured using a TOC analyzer (TOC-VCSH/CSN, Shimadzu).

Two water matrices were used in this study: Milli-Q ultrapure water (UW) and rainwater (RW) collected from Madrid, Spain. Physicochemical analysis revealed that RW had a higher ionic concentration, leading to increased conductivity and total dissolved solids compared to UW. Additionally, RW exhibited a more alkaline pH, ranging from 8.1 to 8.6, in contrast to the nearly neutral pH of UW (Table S2).

3.3. Photocatalytic performance for NOx abatement

This study utilizes a customized NOx photoreactor developed by Maurino et al. [22], which is equipped with a compact 15 mL reaction chamber that ensures airtight operation. Inside the chamber, a UV-transparent polymer turbine facilitates turbulent gas flow with adjustable speed, minimizing the diffusion boundary layer above the catalytic surface. The reactor is designed with uniform LED irradiation and real-time monitoring of gaseous substrates, significantly enhancing photocatalytic performance assessment. The continuously stirred, low-volume setup allows for the precise measurement of the intrinsic photocatalytic activity of the surface under investigation by reducing mass transfer resistance in the gaseous boundary layer adjacent to the solid surface.

The UV light source is positioned external to the reaction chamber, with the fan integrated into the optical path of the LED array to optimize both the system size and gas flow characteristics. The LED array comprises six UV LEDs mounted on an aluminum printed circuit board and powered by a constant current supply. The LEDs are spaced to ensure uniform irradiation across the reactive surface, with adjustable incident UV radiation intensity ranging from 5 to 150 W m^{-2}. The fan speed is variable between 500 and 10,000 rpm, generating a swirling motion in the incoming gas. The coaxial design of the stator enhances turbulent flow within the chamber. Finite element analysis shows that turbulence can be achieved at fan speeds as low as 300 rpm, ensuring precise measurement of intrinsic photocatalytic activity.

NO and NO_2 gas concentrations are continuously monitored using electrochemical sensors (Alphasense models NO-A4 and NO2-A43 F, www.alphasense.com). Environmental parameters such as temperature and humidity are measured with a digital thermohygrometer sensor (Sensirion SHT75). Gaseous substrates are generated from N2 (99.9995%, Nippon Gases), O2 (99.995%, Nippon Gases), and a certified gas mixture containing NO and N2 (107.1 ppmv NO in N_2) using an Entech 4650 dynamic diluter. The 15 mL internal volume of the reactor reaches steady state within 10–30 seconds, with continuous monitoring of key conditions throughout the process. The gas mixture flow rate is maintained at 0.5 L/min. The degradation rate is extrapolated at an infinite fan speed, where the boundary layer thickness approaches zero, removing mass transfer resistance and providing the true intrinsic photoactivity. NOx degradation rates for TiO_2 films are extrapolated based on the inlet gaseous substrate concentration, incident radiant power, LED power, and controlled environmental parameters. The conversion of NO and NOx, NO_2 release, and catalyst selectivity are analyzed using the following equations (Equations (1)-(4)).

$$NO\ conversion\ (\%) \quad = \quad ([NO]_{in} - [NO]_{out})/[NO]_{in} \times\ 100 \tag{1}$$

$$NO_2\ released\ (\%) \quad = \quad ([NO_2]_{out}\ /[NO]_{in})\ \times\ 100 \tag{2}$$

$$NOx\ conversion\ (\%) \quad = \quad ([NO_x]_{in} - [NOx]_{out})/[NOx]_{in}\ \times\ 100 \tag{3}$$

$$\boldsymbol{Selectivuty}, \mathrm{S}(\%) \quad = \quad \frac{\boldsymbol{([NO_x]_{in} - [NOx]_{out})/[NOx]_{in}}}{\boldsymbol{([NO]_{in} - [NO]_{out})/[NO]_{in}}} \times \boldsymbol{100} \tag{4}$$

Deposition of TiO_2 film on Glass

TiO_2 films were prepared by depositing a concentrated (10 g L^{-1}) suspension onto a round glass support using the following steps:

- The glass support was thoroughly washed with water.
- A 10 g L^{-1} TiO_2 suspension in water was prepared and sonicated for 1 hour.
- A 300 µL aliquot of the suspension was applied to the support and evenly spread using the doctor-blade technique to ensure uniform adhesion.
- The film was dried at ambient temperature.
- This process was repeated until the support surface was fully covered.

- Additional layers were applied and dried until a homogeneous thick film was obtained.

4. Results

4.1. Structure Analysis

Figure 2 presents the SEM images of the Na-titanates samples, illustrating the significant impact of pH on the morphological evolution of the initial structures. As the pH varies from 14 to 8, morphologies undergo a substantial transformation, shifting from a platelet-like distorted structure to a more elongated rod-fused structure. This transformation is driven by pH-sensitive nucleation and growth processes, highlighting pH's key role in sodium titanate formation of distinct surface morphologies.

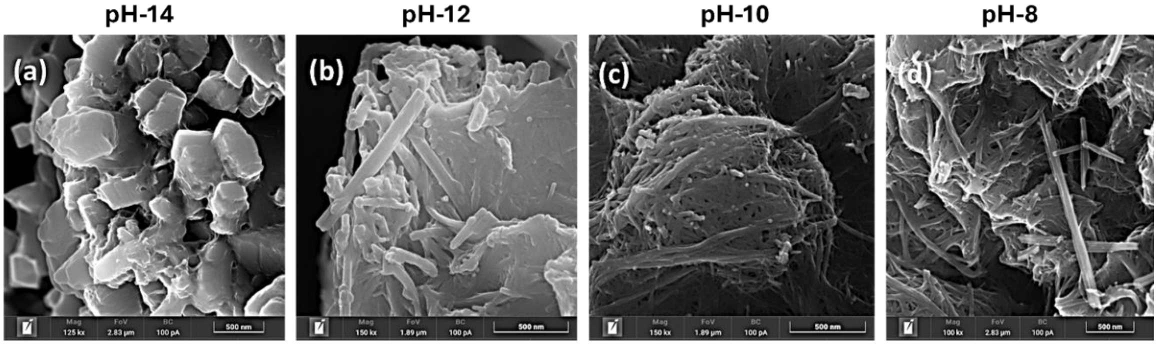

Figure 2. FE-SEM images of Na-titanates prepared under different pH conditions.

Figures 3–4 depict the morphological evolution of TiO_2 nanoparticles synthesized from Na-titanates (at different pH values) upon thermal treatments at 200°C and 230°C. The results reveal a pH- and temperature-dependent restructuring mechanism.

At pH 14, thermal treatment at 200°C and 230°C induced a transformation from platelet-like Na-titanates to a distinct flower-like TiO_2 morphology (Figures 3(a, b)). At 200°C, the specimen (pH14-200°C) exhibited a distorted flower-like structure, while at 230°C, the comparatively higher temperature led to a more compact structure with reduced particle size and a more pronounced flower-like morphology (pH14-230°C). The thermal treatment of Na-titanates at pH 12 promoted the formation of disordered fused nanosheet-like structures, resulting in a disordered morphology (pH 12, 200°C) (Figures 3(c)). However, at 230°C, the increased thermal energy triggered an anisotropic growth mechanism, leading to the self-organization of aloe-vera-like hierarchical structures (pH 12, 230°C) (Figures 3(d)).

For Na-titanates synthesized at pH 10, the relatively lower alkalinity resulted in a mixture of nanorods upon thermal treatment (Figures 4(a, b)). At 200°C, thermal treatment promoted the formation of more uniform nanorods, while at 230°C, the higher thermal energy overcame structural rigidity, facilitating the complete scrolling of nanorods into elongated nanotubes. This transition, driven by increased temperature, enhanced structural reorganization and favored nanotube formation, demonstrating a clear temperature-dependent mechanism.

The pH 8, 200°C specimen exhibited the nucleation of TiO_2 with a mixed nanotube/elongated bipyramidal morphology (Figure 4c). While surface rearrangements were more distinct at 200°C due to a dense population per unit length, increasing the temperature to 230°C resulted in a similar morphology but with a more well-defined shape and larger particle size (Figure 4d). This suggests that lower pH Na-titanates favour kinetically stable TiO_2 morphologies with minimal reorganization, maintaining structural consistency even with temperature variations. The observed structural evolutions are governed by a complex interplay of pH-dependent hydrolysis, and temperature-induced morphologies. These findings highlight the critical influence of alkaline pH and thermal treatment on TiO_2 morphology and phase transformations (discussed in a later section), which, in turn, impact photocatalytic efficiency by modulating surface area, defect density, and charge carrier dynamics [23]. The synergy between morphology and phase composition is further explored in subsequent sections to elucidate their combined impact on photocatalytic performance.

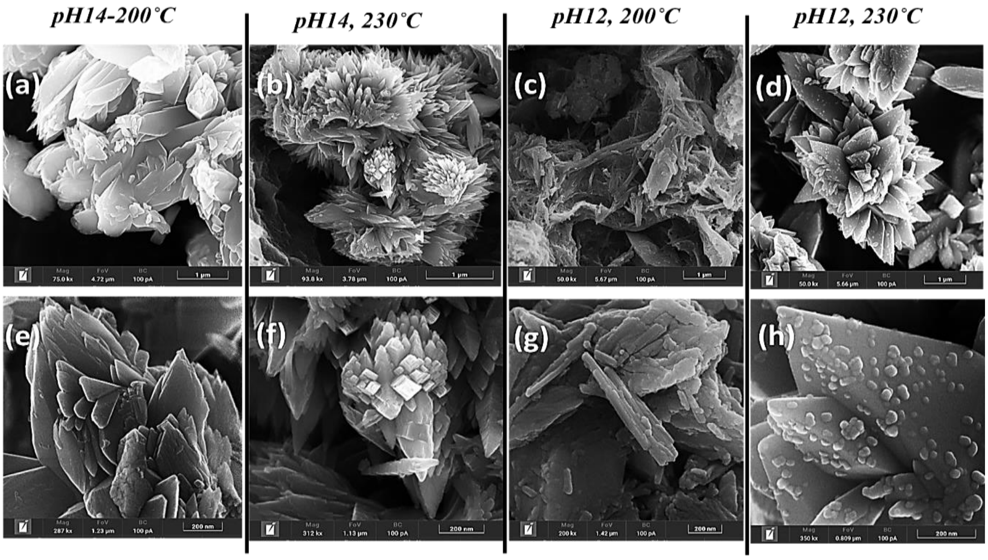

Figure 3. FE-SEM images of TiO_2 derived from Na-titanates at pH 14 and pH 12, after thermal treatment at 200°C and 230°C.

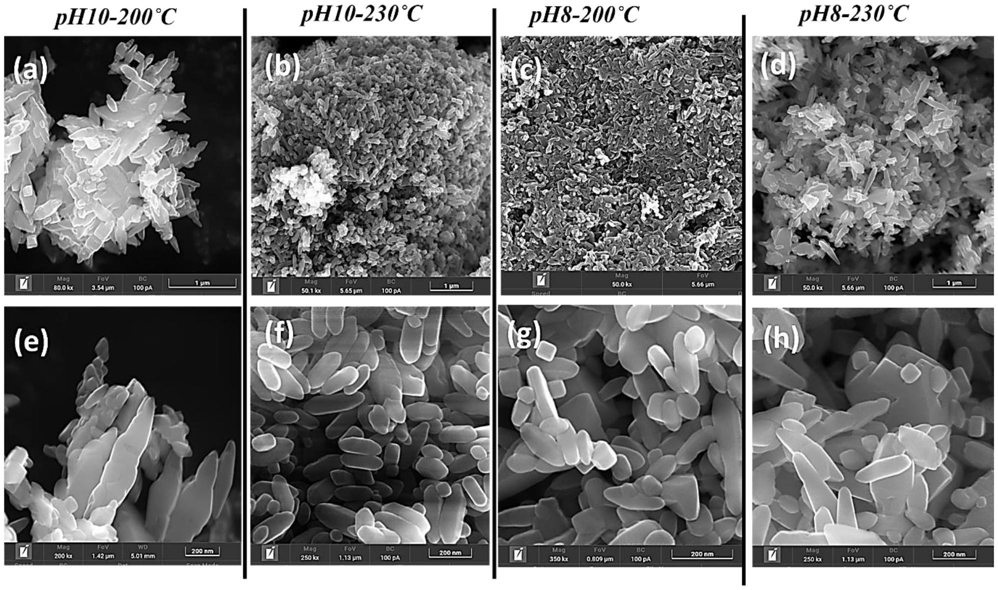

Figure 4. FE-SEM images of TiO_2 derived from Na-titanates at pH 10 and pH 8, after thermal treatment at 200°C and 230°C.

Figure 5 shows the XRD characterization of Na-titanate particles synthesized under controlled pH conditions. The prominent peaks at 2θ values of 28.20° and 48.20° correspond to the characteristic titanate pattern ($Na_2Ti_3O_7$) [ICDD card no. 04-009-1210]. At pH 14, highly alkaline conditions promote the formation of Na_4TiO_4, exhibiting sharp peaks (indicative of Na_4TiO_4) along with broader peaks corresponding to TiO_2 and Ti_2O_3. At lower pH values (8 and 10), the synthesis results in a mixed-phase composition, including $Na_2Ti_3O_7$ and anatase, along with potentially amorphous species. Overall, the XRD profile highlights the influence of pH on phase evolution.

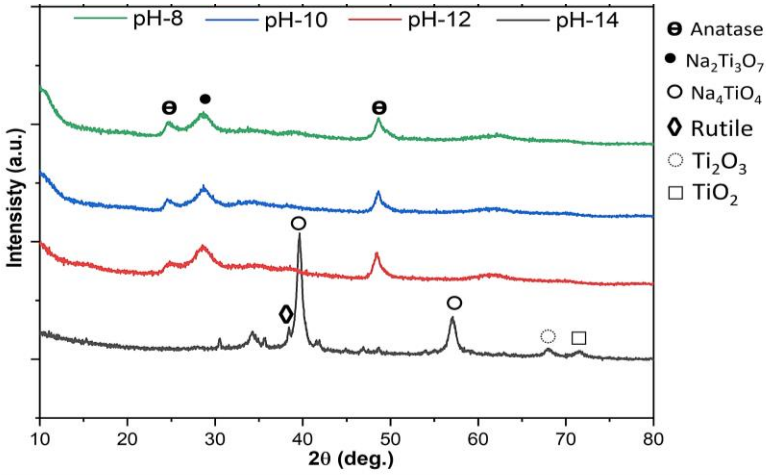

Figure 5. X-ray diffraction patterns of the Na-titanate particles at different adjusted pH values.

Figure 6 presents the XRD spectra of TiO_2 nanomaterials synthesized via hydrothermal treatment at 200°C and 230°C from Na-titanates at pH 8, 10, 12, and 14. The results highlight the critical role of both pH and reaction temperature in governing TiO_2 phase evolution, enabling precise control over anatase and brookite formation. For TiO_2 nanoparticles synthesized at pH 8 and pH 10 after thermal treatment, distinct diffraction peaks at $2\theta = 25.00°$, 37.00°, and 54.00° correspond to the (101), (004), and (211) planes of anatase TiO_2 (ICDD PDF card No. 01-075-2552). These results confirm the successful transformation of Na-titanate precursors into anatase TiO_2, with preferential stabilization of anatase-specific crystal planes. Combined XRD and SEM analyses indicate that moderate alkaline conditions (pH 8–10) favor the nucleation and growth of highly crystalline, phase-pure anatase nanoparticles. In contrast, at higher pH values (12 and 14), the synthesized TiO_2 exhibits diffraction peaks at $2\theta = 25.49°$, 38.19°, and 54.65°, corresponding to the (111), (311), and (421) planes of brookite TiO_2 (ICDD PDF card No. 04-022-2622). The selective formation of brookite under strongly alkaline conditions is attributed to an increased hydroxyl ion concentration, which induces deprotonation and stabilizes brookite-specific lattice planes by modifying the coordination environment of Ti species. Brookite formation occurs at both 200°C and 230°C, suggesting that pH plays a dominant role in phase selectivity, while temperature primarily influences crystallinity and particle growth. These findings highlight the interplay between pH and synthesis temperature in tuning TiO_2 crystalline phases. The hydrothermal synthesis strategy used here effectively tailors TiO_2 phases with distinct crystallographic properties. While temperature plays a limited role in determining the dominant TiO_2 phase under these conditions, it significantly impacts morphological evolution. The relationship between phase composition and morphology is further explored to elucidate their combined influence on photocatalytic performance.

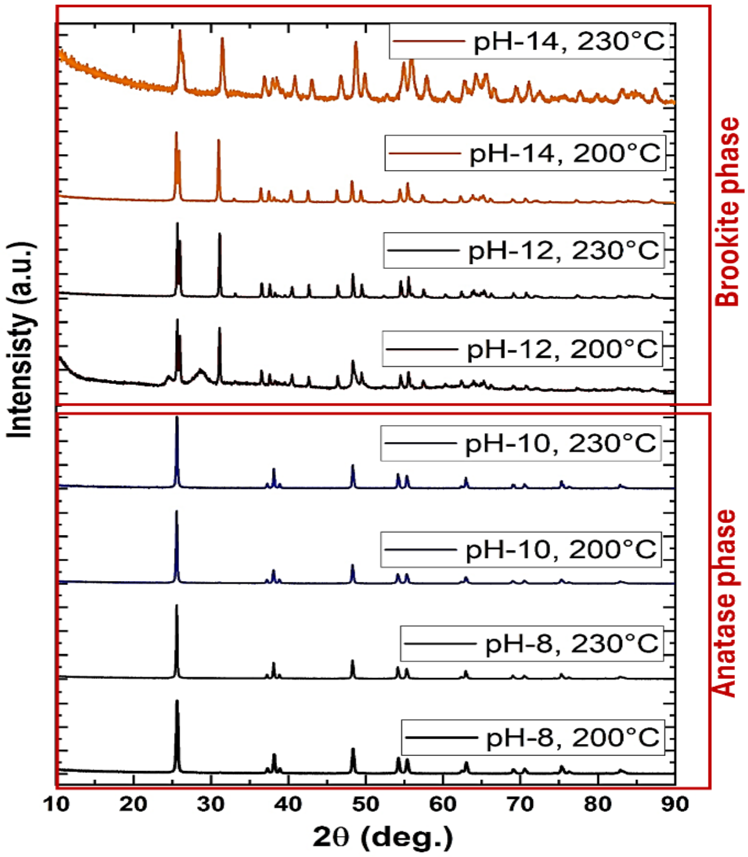

Figure 6. XRD patterns of prepared TiO_2 under different reaction conditions.

Figure 7 presents the UV-Vis absorption analysis of TiO_2 nanoparticles, with bandgap values calculated from Tauc plots. Samples synthesized at pH 8–10 (anatase phase) exhibit a bandgap of ~3.18-3.20 eV, while those at pH 12–14 (brookite phase) show slightly higher values (3.23–3.28 eV). This increase is attributed to structural differences between anatase and brookite, affecting electronic band dispersion and charge carrier dynamics. The slight difference in bandgap between anatase and brookite TiO_2 with varying morphologies is attributed to changes in surface energy, quantum confinement effects, and crystallographic orientation, which influence electron density and charge carrier dynamics. The results highlight the influence of pH on phase composition and optical properties (Table 1), offering tunable electronic characteristics for photocatalytic and optoelectronic applications.

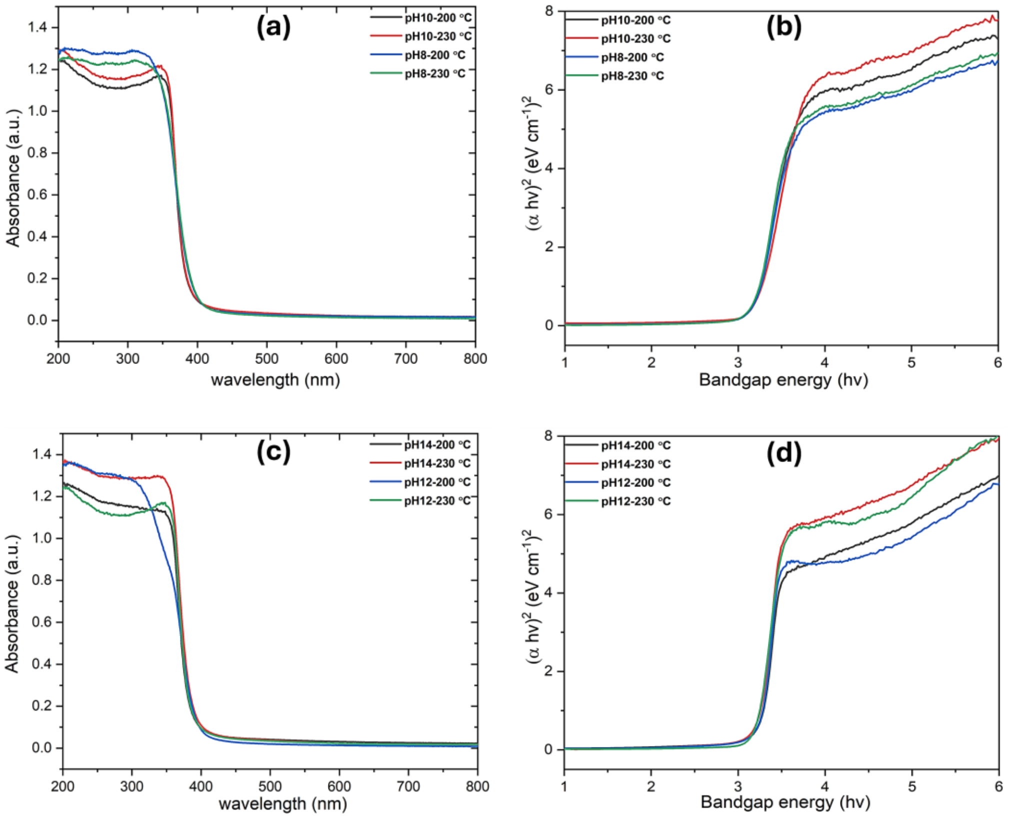

Figure 7. (a, c) UV-VIs absorption spectra, (b, d) Band gap of developed TiO_2 nanoparticles.

Table 1. Band gap energies of developed TiO_2 at various synthetic conditions.

Specimen	Crystallographic form	Band gap energy/eV
pH8-200°C	anatase	3.18
pH8-230°C	anatase	3.16
pH10-200°C	anatase	3.17
pH10-230°C	anatase	3.20
pH12-200°C	Brookite	3.26
pH12-230°C	Brookite	3.23
pH14-200°C	Brookite	3.28
pH14-230°C	Brookite	3.24

4.2. Photocatalytic degradation of aqueous pollutants

The photocatalytic performance of TiO_2 for aqueous degradation was evaluated in two water matrices—Milli-Q water (UW) and highly basic stormwater (SW)—using a fixed pollutant concentration of 0.1 mM. For phenol degradation, TiO_2 samples synthesized at pH 8 (200°C) and pH 10 (230°C) exhibited significantly higher photocatalytic activity compared to those synthesized at pH 10 (200°C) and pH 8 (230°C), despite being primarily anatase (Figure 8). Considering the impact of morphology, TiO_2 specimens with nanotubes and mixed nanotubes/elongated bipyramids showed faster degradation rates, achieving nearly complete phenol removal within 20 minutes in UW and full degradation within 30 minutes in SW for pH-8, 200°C and pH-10, 230°C. The higher TOC removal values of 70% (in UW) and 56% (in SW) for pH-10, 230°C indicate more efficient photocatalytic activity. Higher TOC removal is critical as it reflects the extent of organic pollutant degradation, demonstrating the complete mineralization of contaminants into harmless byproducts like carbon dioxide and water. This suggests that the photocatalyst not only reduces the concentration of pollutants but also contributes to their complete breakdown, ensuring cleaner, safer output in environmental applications.

The distinctive photocatalytic performance among anatase-phase samples is attributed to differences in surface morphology. Fully developed, compact nanotubes and bipyramids (with dense populations and finer sizes) exhibited superior degradation efficiency due to their higher surface area, increased active sites, and enhanced generation of reactive hydroxyl radicals. In contrast, brookite-phase samples showed negligible photocatalytic activity across all morphologies. This is likely due to the lower charge mobility and higher electron-hole recombination rates associated with the brookite phase, significantly reducing the formation of reactive species necessary for pollutant degradation. Additionally, brookite's structural characteristics may hinder its interaction with light, further decreasing its catalytic efficiency under the tested conditions, thus the morphology made no impact on degradation. As a result, brookite samples were excluded from aqueous pollutant degradation studies. Photocatalytic activity in both matrices followed first-order kinetics concerning phenol concentration. First-order rate constants and degradation rates were analyzed using the Langmuir-Hinshelwood model, with results summarized in Table 2.

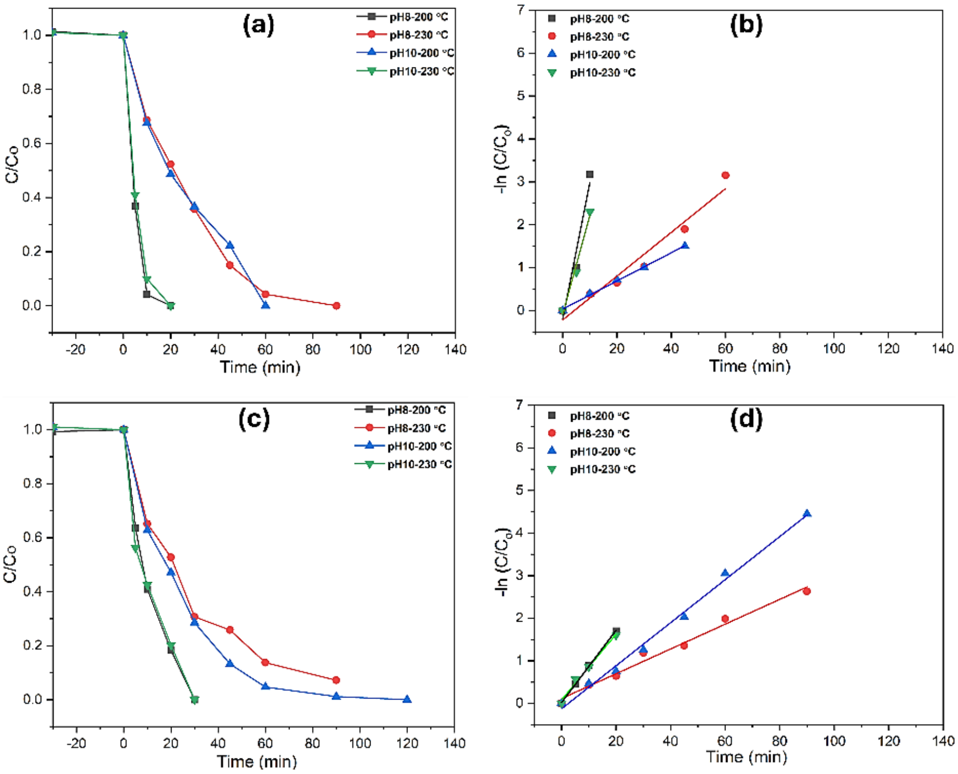

Figure 8. Phenol photodegradation and Pseudo-first order kinetics plots, (a, b) Mili-Q water (UW), (c, d) Rainwater (RW).

Table 2. Constant rate (k) and decomposition rate (χ) of phenol in the presence of TiO_2-based nanoparticles.

Material	Removal Efficiency (%)		Time (min)		K_1		R^2		Normalized Degradation Rate ($M.min^{-1}$)		TOC Removal (%)	
	Mili-Q	Rain Water	Mili-Q	Rain Water	Mili-Q	Rain Water	Mili-Q	Rain Water	Mili-Q	Rain Water	Mili-Q	Rain Water
pH8-200°C	100	100	20	30	0.2943	0.0861	0.9752	0.9995	2.6344	0.6799	61	50
pH8-230°C	100	100	90	90	0.0459	0.0291	0.9743	0.983	0.4405	0.3322	41	35
pH10-200°C	100	100	60	120	0.0339	0.0505	0.9986	0.9816	0.3136	0.5691	30	23
pH10-230°C	100	100	20	30	0.2199	0.0827	0.9911	0.9916	1.6721	0.6374	70	56

Figure 9 illustrates the photodegradation of methomyl using TiO_2 with various morphologies under UV irradiation across different water matrices. Similar to phenol degradation, TiO_2 synthesized at pH 10 (230°C) and pH 8 (200°C) exhibited notable photocatalytic activity, achieving near-complete methomyl removal in 45 and 60 minutes in Milli-Q water (UW), respectively. In contrast, degradation in rainwater (RW) was slower, requiring 90 and 120 minutes for near-complete removal. This delay is likely due to the additional ions and organic matter in RW, which may compete with methomyl for active sites on the catalyst surface, thereby reducing efficiency. Compared to phenol, the methomyl degradation rate is slower. This is due to the more complex structure of methomyl, which contains multiple functional groups, making it more resistant to photocatalytic degradation. Furthermore, methomyl may form more persistent by-products that are difficult to degrade, which slows down the overall degradation process.

For mineralization, total organic carbon (TOC) conversion was significantly higher in UW than in RW after 120 minutes of UV exposure. Specifically, the TiO_2 samples synthesized at pH 10 (230°C) and pH 8 (200°C) achieved 57% and 46% TOC conversion in UW, respectively, indicating effective mineralization of methomyl into CO_2 and H_2O. However, in RW, mineralization efficiency was lower, with TOC conversions of 41% and 29%, suggesting that the RW matrix promotes the formation of more persistent by-products, which are more challenging to completely mineralize.

Notably, the TiO_2 synthesized at pH 10 (230°C) exhibited higher TOC conversion than pH 8 (200°C), demonstrating its superior performance in mineralizing methomyl. This can be attributed to the more optimized surface area and active sites of the anatase-phase structure formed at pH 10 (230°C), which enhances both pollutant degradation and mineralization efficiency. The higher TOC conversion observed for the pH 10 (230°C) TiO_2 further emphasizes the importance of tailoring synthesis conditions, such as pH and temperature, to enhance photocatalytic efficiency. Other morphologies, such as those formed under pH 8 (230°C) and pH 10 (200°C), exhibited relatively lower photocatalytic performance, likely due to less optimal surface structures that offer reduced surface area and active sites for degradation.

The apparent first-order rate constants (k_{pest}) for methomyl degradation in both water matrices are provided in Table 3, with high r^2 values (0.9194–0.9996) confirming the suitability of the first-order kinetic model for describing methomyl degradation under both UW and RW conditions.

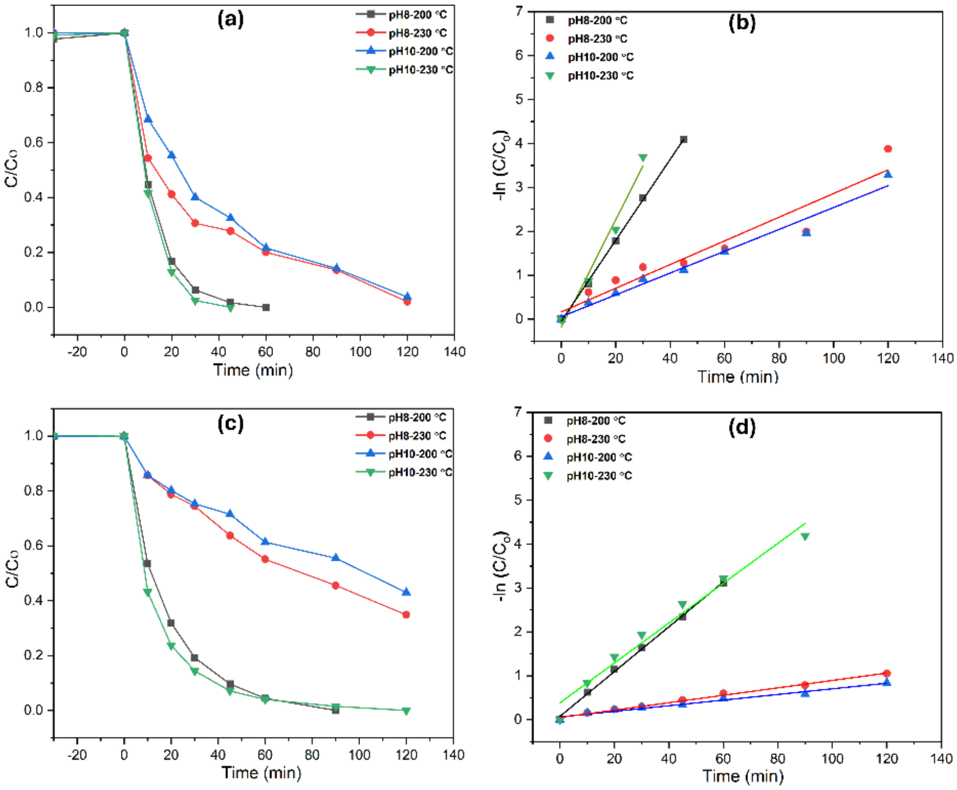

Figure 9. Methomyl photodegradation and Pseudo-first order kinetics plots, (a, b) Mili-Q water (UW), (c, d) Rainwater (RW).

Table 3. Constant rate (k) and decomposition rate (χ) of Methomyl in the presence of TiO_2-based nanomaterials.

Material	Removal Efficiency (%)		Time (min)		K_1		R^2		Normalized Degradation Rate ($M.min^{-1}$)		TOC Removal (%)	
	Mili-Q	Rain Water	Mili-Q	Rain Water	Mili-Q	Rain Water	Mili-Q	Rain Water	Mili-Q	Rain Water	Mili-Q	Rain Water
pH8-200°C	100	100	60	90	0.0907	0.051	0.9996	0.998	1.498	0.754	46	29
pH8-230°C	98	65	120	120	0.027	0.0091	0.9194	0.9941	0.386	0.142	32	19
pH10-200°C	96	57	120	120	0.0256	0.0072	0.9894	0.9844	0.366	0.113	25	16

pH10-230°C	100	100	45	120	0.0992	0.0454	0.9966	0.9721	1.567	0.653	57	41

Figure 10 illustrates the photodegradation of diclofenac (DCF) under UV irradiation in both mili-Q water (UW) and rainwater (RW), revealing a degradation trend similar to that of phenol and methomyl. The degradation rate was significantly higher in UW, with anatase-phase TiO_2 synthesized at pH 10 (230°C) and pH 8 (200°C) demonstrating the highest photocatalytic efficiency. In UW, nearly complete DCF degradation was achieved within 30 minutes, whereas in RW, TiO_2 synthesized at pH 10 (230°C) reached full degradation in 45 minutes, and the pH 8 (200°C) sample required 60 minutes.

The mineralization efficiency, measured by TOC conversion, was notably higher in UW than in RW, highlighting the simpler composition of UW, which facilitates more complete breakdown of organic pollutants. Specifically, anatase-phase TiO_2 synthesized at pH 10 (230°C) achieved up to 78% TOC removal in UW within 120 minutes, compared to 66% in RW. Kinetic analysis using a modified Langmuir-Hinshelwood model confirmed that degradation followed first-order kinetics in both matrices. The first-order rate constants for DCF degradation further underscore the influence of pH-induced phase transitions in TiO_2 (Table 4). Anatase-phase TiO_2 exhibited superior photocatalytic activity, contributing to more efficient mineralization. The degradation pathway of DCF follows sequential transformations into hydroxy- and dihydroxy-diclofenac derivatives, which then undergo further transformations into chloro- or hydroxyl-phenol intermediates. These intermediates are eventually mineralized through processes like ring opening, ultimately converting into carboxylic acids.

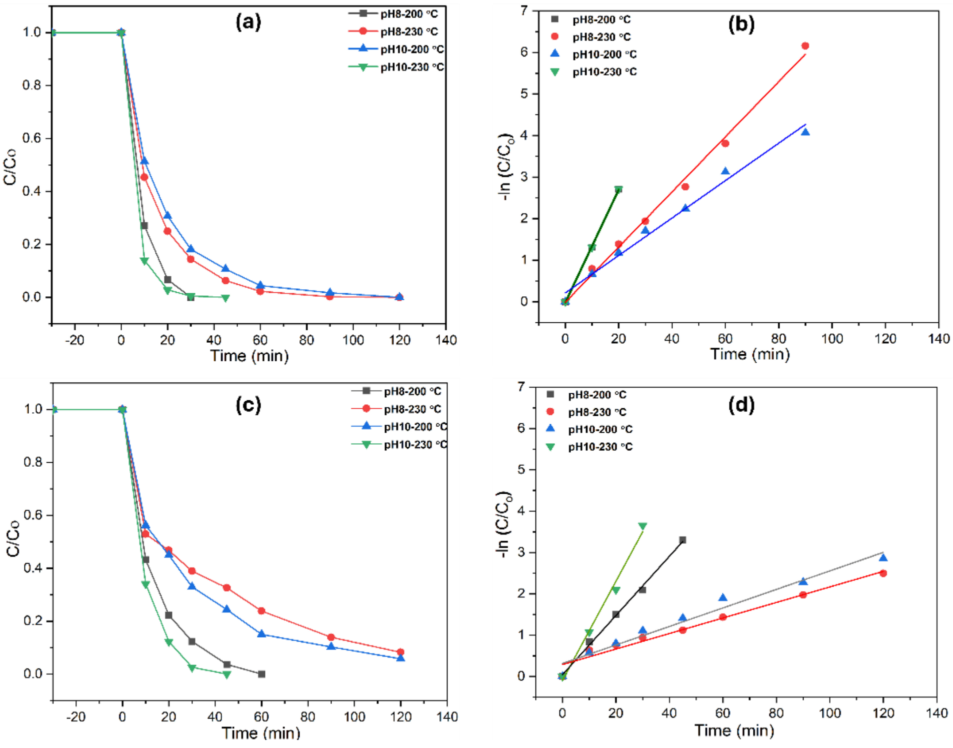

Figure 10. Diclofenac photodegradation and Pseudo-first order kinetics plots, (a, b) Mili-Q water (UW), (c, d) Rainwater (RW).

Preprints.org (www.preprints.org) | NOT PEER-REVIEWED | Posted: 23 March 2025 doi:10.20944/preprints202503.1649.v1

Table 4. Pseudo first order rate constant (k) and decomposition rate (χ) of Diclofenac in the presence of TiO$_2$-based nanomaterials.

Material	Removal Efficiency (%)		Time (min)		K_1		R^2		Normalized Degradation Rate (M.min^{-1})		TOC Removal (%)	
	Mili-Q	Rainwater	Mili-Q	Rainwater	Mili-Q	Rainwater	Mili-Q	Rainwater	Mili-Q	Rainwater	Mili-Q	Rainwater
pH8-200°C	100	100	30	60	0.1348	0.073	0.9998	0.9987	2.107	1.917	57	43
pH8-230°C	100	92	90	120	0.0662	0.0171	0.998	0.9972	1.860	0.490	24	20
pH10-00°C	100	94	120	120	0.045	0.0224	0.9872	0.9669	1.245	0.625	43	31
pH10-30°C	100	100	30	45	0.1813	0.116	0.9994	0.9954	3.230	3.010	78	66

The significant differences in photocatalytic performance among TiO$_2$ samples can be attributed to the interplay between morphology, phase composition, and the consistently observed anatase phase in the pH 8–10 range. While the anatase phase dominates across all these pH conditions, variations in morphology—such as surface area, population density, and exposed crystal facets—play a critical role in determining photocatalytic efficiency. TiO$_2$ synthesized at pH 8 (200°C) and pH 10 (230°C) showed superior photocatalytic activity, mainly due to their unique morphologies. The sample synthesized at pH 10 (230°C), which forms nanotubes and mixed nanotubes/elongated bipyramids, has a higher surface area and more accessible active sites, improving interaction with pollutants and boosting degradation efficiency. Similarly, the bipyramidal morphology observed at pH 8 (200°C) exhibited comparable photocatalytic performance, highlighting the importance of morphology even when the crystal phase remains unchanged.

The Total Organic Carbon (TOC) values further reinforce the significance of these morphological variations. Higher TOC removal rates were observed for TiO$_2$ synthesized at pH 10 (230°C), indicating more complete mineralization of pollutants into CO$_2$ and H$_2$O. This suggests that the optimized surface area and active site accessibility in these morphologies enhance the overall breakdown of organic contaminants. TiO$_2$ synthesized under other conditions with less favorable morphologies exhibited comparatively lower TOC values, indicating reduced pollutant mineralization efficiency. This limitation is primarily due to their lower capacity for reactive oxygen species (ROS) generation and inefficient charge carrier separation, ultimately hindering their overall photocatalytic performance. This is indicative of the crucial role that surface characteristics play in not just the degradation of pollutants but also in their mineralization, which is essential for complete pollutant removal.

These findings underscore the critical synergy between phase composition, morphology, and TOC values in optimizing photocatalytic materials. By controlling not only the crystallographic phase but also the shape and surface characteristics of TiO_2 nanostructures, it becomes possible to enhance photocatalytic efficiency, as demonstrated by TiO_2 synthesized at pH 10 (230°C), which showed the highest TOC removal and the most efficient degradation of organic pollutants. This material, featuring a nanorod morphology, emerges as an ideal candidate for advanced photocatalytic applications.

4.3. Photocatalytic NOx Abatement

This study systematically investigates the photoconversion of nitrogen oxides (NOx) using TiO_2-based photocatalysts of two distinct phases, anatase and brookite. The impact of varying fan speeds (500–4000 rpm) on boundary layer thickness, mass transfer, and NO photodegradation is thoroughly examined in a custom-designed photoreactor. This approach enables a comparative analysis of the selective phases and morphologies, providing deeper insights into their photocatalytic efficiency and selectivity for NOx abatement (Figure 11). Higher fan speeds reduce the boundary layer thickness, minimizing mass transfer resistance and allowing for more efficient NO transport to the catalyst surface. This results in accelerated reaction rates and improves overall conversion efficiency.

For comparative analysis, TiO_2 synthesized at pH 10 (230°C) was selected due to its superior performance in aqueous pollutant degradation, making it an ideal candidate for evaluating NOx abatement efficiency. Meanwhile, the brookite-based specimen synthesized at pH 12 (200°C) was chosen after initial screening for its distinct response in air pollutant degradation, allowing a systematic comparison of phase-dependent photocatalytic performance. Under LED irradiation at 20 W/m^2, anatase-phase TiO_2 (pH-10, 230°C) achieved approximately 78% NO conversion efficiency, with degradation rates of 0.427 $mg{\cdot}min^{-1}{\cdot}m^{-2}$ for NO and 0.578 $mg{\cdot}min^{-1}{\cdot}m^{-2}$ for NOx. Although anatase-phase TiO_2 demonstrated high NO conversion efficiency, it released more NO_2 (16%) than brookite-phase TiO_2 (pH-12, 200°C), indicating that it is less selective in NOx abatement. This selectivity is a crucial factor in improving urban air quality. Brookite-phase TiO_2 (pH-12, 200°C) demonstrated high NO conversion (~60%) with remarkable selectivity (~91%) and minimal NO_2 release (3–4%), (Figure 12). This distinctive performance in NOx abatement, despite its comparatively lower efficiency in aqueous pollutant degradation, makes brookite-phase TiO_2 significant for air pollution control. Furthermore, brookite-phase TiO_2 showed a continuous increase in NO degradation efficiency even at decreasing fan speeds down to 100 rpm, after which the reaction rate plateaued. This suggests that at lower fan speeds (100–500 rpm), mass transfer is the limiting factor, while at higher speeds, reaction kinetics dominate. Thus, brookite-phase TiO_2 maintained excellent selectivity towards NOx degradation products and minimized NO_2 formation—an essential characteristic for optimizing deNOx processes in gas-phase applications. The comparison between anatase-phase TiO_2 (pH 10, 230°C) and brookite-phase TiO_2 (pH 12, 200°C) underscores the importance of phase engineering in determining photocatalytic efficiency. Anatase-phase TiO_2 (pH-10, 230°C) excelled in aqueous pollutant degradation, while brookite-phase TiO_2 demonstrated superior selectivity in NOx abatement, achieving higher selectivity and lower NO_2 release. This highlights the critical role of phase and morphology in optimizing TiO_2-based photocatalysts for different environmental applications.

In summary, this study emphasizes the significance of phase-engineered TiO_2 in photocatalytic applications, with anatase-phase TiO_2 excelling in aqueous pollutant degradation and brookite-phase

TiO_2 performing remarkably well in NOx abatement. The interplay between morphology, crystallographic phase, and mass transfer dynamics is crucial for optimizing photocatalytic performance, and the results further emphasize the importance of selecting the appropriate phase and morphology for targeted environmental applications, particularly for air pollution control.

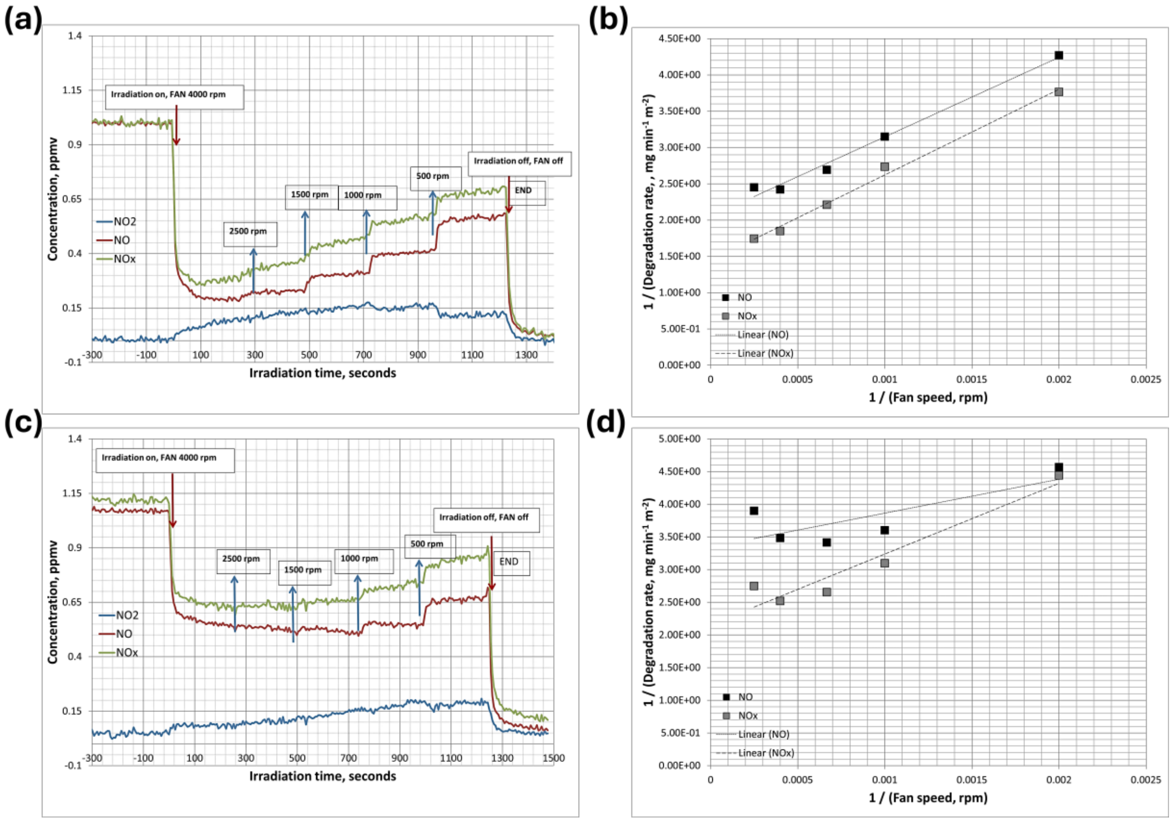

Figure 11. Nitrogen oxide profiles and Plot of the NO/NOx degradation rate vs fan speed obtained during the photodegradation of gaseous NO under UV irradiation (20 Wm^{-2}), (a, b) pH-10, 230 °C, (c, d) pH-12, 200 °C: The plots refer to the same measurement: 1 ppmv NO nominal initial concentration, 54% relative humidity.

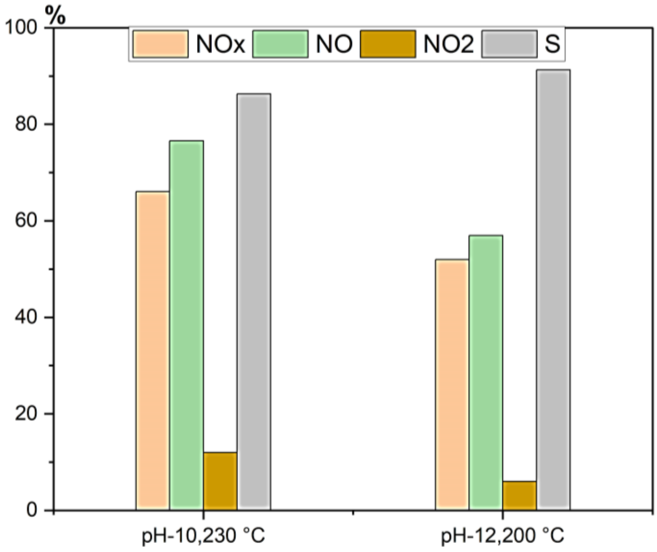

Figure 12. NO, NOx conversions, NO_2 release and “selectivity” values for the 20 Wm^{-2} lamp.

5. Discussion

doi:10.20944/preprints202503.1649.v1

This study underscores the critical role of phase engineering and morphology in optimizing the photocatalytic performance of TiO_2 nanoparticles synthesized through hydrothermal methods under controlled pH and temperature conditions. Anatase-phase TiO_2, particularly in its nanotube/bipyramid morphology, demonstrates significant efficiency in aqueous-phase pollutant degradation. Its high surface area, superior crystallinity, and enhanced charge separation facilitate efficient pollutant conversion, including phenol, methomyl, and diclofenac, with the highest total organic carbon (TOC) removal observed. Water matrix composition also influences degradation kinetics, with ultrapure water (UW) showing the fastest degradation and highest TOC removal (~79%), while methomyl degradation occurs at a slower rate due to its more complex structure [19,20].

In contrast, brookite-phase TiO_2 synthesized at pH 12 (200°C), despite showing negligible activity for aqueous pollutant degradation, excels in NOx abatement selectivity. This phase's unique crystallographic structure enhances NO_2 adsorption and conversion efficiency, resulting in high NO conversion (~60%) with remarkable selectivity (~91%) and minimal NO_2 release (~3–4%). These characteristics make brookite-phase TiO_2 ideal for air pollution control, especially in urban environments. The comparison between anatase-phase TiO_2 (pH 10, 230°C) and brookite-phase TiO_2 (pH 12, 200°C) highlights the distinct advantages of each phase for different applications. Anatase-phase TiO_2 is highly effective for aqueous-phase pollutant degradation and air-phase NOx abatement. In contrast, brookite-phase TiO_2 stands out in NOx removal, particularly for its selectivity in minimising NO_2 release. The generic mechanism of NOx abatement can be as follows (Equation 5-10),[24,25]:

$$TiO_2 + h\nu \rightarrow e^- + h^+ \tag{5}$$

$$e^- + O_2 \rightarrow O_2{\cdot}^- \tag{6}$$

$$h^+ + H_2O \rightarrow \cdot OH \tag{7}$$

$$NO + \cdot OH \rightarrow HNO_2 \tag{8}$$

$$HNO_2 + OH \rightarrow NO_2 \tag{9}$$

$$NO_2 + OH \rightarrow HNO_3 \tag{10}$$

6. Conclusions

In conclusion, this study underscores the pivotal role of phase engineering and morphology in optimizing the photocatalytic performance of TiO_2 nanoparticles for environmental remediation. By systematically tailoring the synthesis conditions, including pH and temperature, TiO_2 nanostructures with distinct phases and morphologies were developed, demonstrating remarkable versatility in pollutant degradation. Anatase-phase TiO_2, particularly with nanotube morphology, exhibited significant efficiency in aqueous-phase pollutant degradation, achieving high reaction rates and complete degradation of phenol, methomyl, and diclofenac. In contrast, brookite-phase TiO_2, while showing negligible performance in liquid-phase applications, excelled in NOx abatement, achieving relevant NO conversion with high selectivity and minimal NO_2 release. Future research may focus on enhancing these properties further through doping strategies, such as incorporating noble metals, to promote photocatalyst activity. This approach could pave the way for next-generation photocatalytic technologies that effectively address diverse pollution challenges, from water contamination to atmospheric NOx reduction.

Supplementary Materials: The following supporting information can be downloaded at the website of this paper posted on Preprints.org.

Funding: V. Maurino kindly acknowledges funding by Regione Piemonte, Italy, through the project ECOBRAKE “Studio e Sviluppo di materiali frenanti ecologici e a bassa emissione di particolato per applicazioni automotive”—L.R. 34/2004—D.D. n° 409 del 02/11/2021. D. Hermosilla is grateful to Grant PID2020-114918RB-I00 (Project PHOTOPREBIO) funded by MCIN/AEI/10.13039/501100011033. MA Iqbal is grateful for the support of the European project UNA4CAREER (Marie Skłodowska Curie grant No 847635).

Conflicts of Interest: The authors declare no conflict of interest.

References

1. Bell, K. Y.; Wells, M. J.; Traexler, K. A.; Pellegrin, M. L.; Morse, A.; Bandy, J. Emerging pollutants. *WER* **2011** *83*, 1906-1984. https://doi.org/10.2175/106143011X13075599870298.
2. Deblonde, T.; Cossu-Leguille, C.; Hartemann, P. Emerging pollutants in wastewater: a review of the literature. *Int. J. Hyg. Environ* **2011** *214*, 442-448. https://doi.org/10.1016/J.IJHEH.2011.08.002.
3. Mohapatra, L.; Parida, K. A review on the recent progress, challenges and perspective of layered double hydroxides as promising photocatalysts. *J. Mater. Chem. A* **2016** 28, 10744-10766. https://doi.org/10.1039/C6TA01668E.
4. Pandey, S. K.; Singh, J. Nitrogen dioxide: Risk assessment, environmental, and health hazard. *Hazardous Gases* **2021** 273-288. Academic Press.
5. Huang, S.; Li, H.; Wang, M.; Qian, Y.; Steenland, K.; Caudle, W. M.; Shi, L. Long-term exposure to nitrogen dioxide and mortality: A systematic review and meta-analysis. *Sci. Total Environ* **2021** *776*, 145968. https://doi.org/10.1016/J.SCITOTENV.2021.145968.
6. Blake, D. M.; Webb, J.; Turchi, C.; Magrini, K.; Kinetic. Mechanistic overview of TiO_2-photocatalyzed oxidation reactions in aqueous solution. *Sol. Energy Mater* **1991** *24*, 584-593. https://doi.org/10.1016/0165-1633(91)90092-Y.
7. Schneider, J.; Matsuoka, M.; Takeuchi, M.; Zhang, J.; Horiuchi, Y.; Anpo, M., Bahnemann, D. W. Understanding TiO_2 photocatalysis: mechanisms and materials. *Chem. Rev* **2014** *114*, 9919-9986. https://doi.org/10.1021/CR5001892.
8. Iqbal, M. A.; Asghar, H.; Maurino, V.; Matykina, E.; Arrabal, R.; Mohedano, M. Evaluating the energy consumption, structural, and corrosion resistance properties of photocatalytic TiO_2-based PEO coatings on pre-anodized AA2024-Al. *J. Surf* **2024** *44*, 103659.
9. Basavarajappa, P. S.; Patil, S. B.; Ganganagappa, N.; Reddy, K. R.; Raghu, A. V.; Reddy, C. V. Recent progress in metal-doped TiO2, non-metal doped/codoped TiO_2 and TiO_2 nanostructured hybrids for enhanced photocatalysis. *Int. J. Hydrogen Energy* **2020** *45*, 7764-7778. https://doi.org/10.1016/j.ijhydene.2019.07.241.
10. Bucharsky, E. C.; Schell, G.; Oberacker, R.; Hoffmann, M. J. Anatase–rutile transformation in TiO_2–V_2O_5 catalyst coatings for ceramic foams. *J. Eur. Ceram* **2009** *29*, 1955-1961. https://doi.org/10.1016/J.JEURCERAMSOC.2008.12.007.
11. Yang, Y.; Hu, J. X.; Liang, Y.; Zou, J. P.; Xu, K.; Hu, R. J.; Yuan, C. L. Anatase TiO_2 hierarchical microspheres consisting of truncated nanothorns and their structurally enhanced gas sensing performance. *J. Alloys Compd* **2017** *694*, 292-299. https://doi.org/10.1016/J.JALLCOM.2016.09.328.
12. Chen, D.; Cheng, Y.; Zhou, N.; Chen, P.; Wang, Y.; Li, K.; Ruan, R. Photocatalytic degradation of organic pollutants using TiO_2-based photocatalysts: A review. *J. Clean. Prod* **2020** *268*, 121725. https://doi.org/10.1016/J.JCLEPRO.2020.121725.
13. Eskandarloo, H.; Zaferani, M.; Kierulf, A.; Abbaspourrad, A. Shape-controlled fabrication of TiO_2 hollow shells toward photocatalytic application. *Appl. Catal. B: Environ* **2018** *227*, 519-529. https://doi.org/10.1016/J.APCATB.2018.01.059.
14. Maisano, M.; Dozzi, M. V.; Selli, E. Searching for facet-dependent photoactivity of shape-controlled anatase TiO2. *J. Photochem. Photobiol* **2016** *28*, 29-43. https://doi.org/10.1016/J.JPHOTOCHEMREV.2016.07.002.
15. Pantaleone, S.; Pellegrino, F.; Maurino, V.; Corno, M.; Ugliengo, P.; Mino, L. Disclosing the true atomic structure of {001} facets in shape-engineered TiO_2 anatase nanoparticles. *J. Mater. Chem. A* **2024** *12*, 4325-4332. https://doi.org/10.1039/D3TA06694K.
16. D’Arienzo, M.; Carbajo, J.; Bahamonde, A.; Crippa, M.; Polizzi, S.; Scotti, R.; Morazzoni, F. Photogenerated defects in shape-controlled TiO_2 anatase nanocrystals: a probe to evaluate the role of crystal facets in photocatalytic processes. *J. Am. Chem. Soc* **2011** *133*, 17652-17661. https://doi.org/10.1021/ja204838s.
17. Li, J.; Yu, Y.; Chen, Q.; Li, J.; Xu, D. Controllable synthesis of TiO_2 single crystals with tunable shapes using ammonium-exchanged titanate nanowires as precursors. *Cryst. Growth Des* **2010** *10*, 2111-2115. https://doi.org/10.1021/cg9012087.

doi:10.20944/preprints202503.1649.v1

18. Liu, N.; Zhao, Y.; Wang, X.; Peng, H.; Li, G. Facile synthesis and enhanced photocatalytic properties of truncated bipyramid-shaped anatase TiO_2 nanocrystals. *Mater. Lett* **2013** *102*, 53-55. https://doi.org/10.1016/J.MATLET.2013.03.106.
19. Asghar, H.; Hermosilla, D.; Gascó, A.; Maurino, V.; Iqbal, M. A. Exploring the Photocatalytic Efficiency of Heterostructured TiO_2 Nanobelts for Emerging Liquid Contaminants in Different Water Matrices. *Separations*, **2025** *12*, 49. https://doi.org/10.3390/SEPARATIONS12020049/S1.
20. Asghar, H.; Hermosilla, D.; Pellegrino, F.; Muelas-Ramos, V.; de Los Ríos, C.; Gascó, A.; Iqbal, M. A. From Anatase TiO_2 Nano-Cuboids to Nano-Bipyramids: Influence of Particle Shape on the TiO2 Photocatalytic Degradation of Emerging Contaminants in Contrasted Water Matrices. *Molecules*, **2025** *30*, 424. https://doi.org/10.3390/MOLECULES30020424/S1.
21. Kamran, M.; Kandiel, T. A.; Abdel, A, S.; Morsy, M. A.; Bahnemann, D. W. Mechanistic Insights into the High Selectivity and Photocatalytic Activity of Brookite TiO_2 toward NO_x Abatement. *J. Phys. Chem. C* **2023** *127*, 7707-7717. https://doi.org/10.1021/acs.jpcc.3c01734.
22. Pellegrino, F.; Zangirolami, M.; Minero, C.; Maurino, V. Portable photoreactor for on-site measurement of the activity of photocatalytic surfaces. *Catal. Today* **2020** *340*, 363-368. https://doi.org/10.1016/J.CATTOD.2018.09.023.
23. Wadge, M. D.; McGuire, J.; Thomas, K. G.; Stuart, B. W.; Felfel, R. M.; Ahmed, I.; Grant, D. M. Developing alkaline titanate surfaces for medical applications. *Int. Mater. Rev* **2023** *68*, 677-724. https://doi.org/10.1080/09506608.2022.2153217.
24. Rhimi, B.; Padervand, M.; Jouini, H.; Ghasemi, S.; Bahnemann, D. W.; Wang, C. Recent progress in NOx photocatalytic removal: Surface/interface engineering and mechanistic understanding. *J. Environ. Chem. Eng* **2022** *10*, 108566. https://doi.org/10.1016/J.JECE.2022.108566.
25. Ângelo, J.; Andrade, L.; Madeira, L. M.; Mendes, A. An overview of photocatalysis phenomena applied to NOx abatement. *JEM* **2013** *129*, 522-539. https://doi.org/10.1016/J.JENVMAN.2013.08.006.